

AD-A282 300



REF ID: A6566  
Rome Laboratory  
Griffiss Air Force Base

## CLUTTER SIGNAL POLARIZATION IN BISTATIC RADAR: EFFECT OF ANTENNA SIDELOBE CLUTTER

David S. Fallon, Captain, USAF (Rome Laboratory)  
J. Leon Poirier (Horizons Technology Inc.)

DTIC  
ELECTE  
JUL 20 1994  
S G D

APPROVED FOR PUBLIC RELEASE; DISTRIBUTION UNLIMITED.

94-22609  
SAC

Rome Laboratory  
Air Force Materiel Command  
Griffiss Air Force Base, New York

DTIC QUALITY INSPECTED 1

This report has been reviewed by the Rome Laboratory Public Affairs Office (PA) and is releasable to the National Technical Information Service (NTIS). At NTIS it will be releasable to the general public, including foreign nations.

RL-TR-94-106 has been reviewed and is approved for publication.

APPROVED:



JOHN F. LENNON  
Chief, Applied Electromagnetics Division

FOR THE COMMANDER:



ROBERT V. MCGAHAN  
Director of Electromagnetics & Reliability

If your address has changed or if you wish to be removed from the Rome Laboratory mailing list, or if the addressee is no longer employed by your organization, please notify RL ( ERCE ) Hanscom AFB MA 01731. This will assist us in maintaining a current mailing list.

Do not return copies of this report unless contractual obligations or notices on a specific document require that it be returned.

# REPORT DOCUMENTATION PAGE

Form Approved  
OMB No. 0704-0188

Public reporting burden for this collection of information is estimated to average 1 hour per response, including the time for reviewing instructions, searching existing data sources, gathering and maintaining the data needed, and completing and reviewing the collection of information. Send comments regarding this burden estimate or any other aspect of this collection of information, including suggestions for reducing this burden, to Washington Headquarters Services, Directorate for Information Operations and Reports, 1215 Jefferson Davis Highway, Suite 1204, Arlington, VA 22202-4302, and to the Office of Management and Budget, Paperwork Reduction Project (0704-0188), Washington, DC 20503.

1. AGENCY USE ONLY (Leave blank)			2. REPORT DATE MAY 1994	3. REPORT TYPE AND DATES COVERED INHOUSE November 1993 - May 1994	
4. TITLE AND SUBTITLE <b>CLUTTER SIGNAL POLARIZATION IN BISTATIC RADAR: EFFECT OF ANTENNA SIDELOBE CLUTTER</b>			5. FUNDING NUMBERS PE: 62702F PROJ NO: 4600 TASK NO: 15 WORK UNIT: 13		
6. AUTHOR(S) DANIEL S. FALLON, CAPT, USAF J. LEON POIRIER*			8. PERFORMING ORGANIZATION REPORT NUMBER RL-TR-94-106		
7. PERFORMING ORGANIZATION NAME(S) AND ADDRESS(ES) ROME LABORATORY/ERC 31 GRENIER STREET HANSCOM AFB, MA 01731-3010			9. SPONSORING/MONITORING AGENCY NAME(S) AND ADDRESS(ES)		
11. SUPPLEMENTARY NOTES  *Horizons Technology Inc., Billerica, MA			10. SPONSORING/MONITORING AGENCY REPORT NUMBER		
12a. DISTRIBUTION/AVAILABILITY STATEMENT  APPROVED FOR PUBLIC RELEASE; DISTRIBUTION UNLIMITED			12b. DISTRIBUTION CODE		
13. ABSTRACT (Maximum 200 words)  Sidelobe contributions to a radar signal's polarization may distort the polarization of clutter originating in the mainbeam. To assure that radar clutter polarization measurements are accurate and that polarization nulling algorithms under consideration would work properly, it is necessary to analyze the contributions of antenna sidelobe clutter to signal polarization. This report considers two bistatic radar configurations over homogeneous terrain. The terrain is represented by the two-scale-of-roughness bistatic scattering model. Two antenna models are used, one a square aperture, and the other a simple approximation to a circular aperture with adjustable sidelobe levels. The results for the square aperture show a small change in the signal polarization from the mainbeam-only value when the sidelobes are added in. For the adjustable sidelobe level antenna the sidelobe corruption is small until the uniform sidelobe level reaches -20 dB.					
14. SUBJECT TERMS Bistatic radar Polarization Sidelobe clutter			15. NUMBER OF PAGES 34		16. PRICE CODE
17. SECURITY CLASSIFICATION OF REPORT Unclassified		18. SECURITY CLASSIFICATION OF THIS PAGE Unclassified		19. SECURITY CLASSIFICATION OF ABSTRACT Unclassified	
20. LIMITATION OF ABSTRACT SAR					

## Contents

1. INTRODUCTION	1
2. POLARIZATION	2
3. CLUTTER CROSS SECTION	7
4. RADAR GEOMETRIES	12
5. ANTENNA PATTERNS	18
6. CALCULATIONS AND RESULTS	20
7. CONCLUSIONS	26
REFERENCES	27

Accesion For	
NTIS	CRA&I <input checked="" type="checkbox"/>
DTIC	TAB <input type="checkbox"/>
Unannounced	<input type="checkbox"/>
Justification .....	
By .....	
Distribution /	
Availability Codes	
Dist	Avail and / or Special
A-1	

## Illustrations

1. Electric Field Orientation	2
2. Elliptically Polarized Field	4
3. Poincaré Sphere	5
4. Projection of Poincaré Sphere onto Equatorial Plane	5
5. Bistatic Scattering Geometry	7
6. Co-Polarized Component of the Scattered Electric Field	11
7. Cross-Polarized Component of the Scattered Electric Field	11
8. Bistatic Radar Geometry	12
9. Radar Geometry One. Approximates experimental clutter measurement setup	13
10. Incident and Scattering Angles for Geometry One	14
11. Radar Geometry Two	15
12. Incident and Scattering Angles for Geometry Two	15
13. Square Aperture Antenna Pattern	19
14. Variable Sidelobe Level Antenna Pattern	19
15. Polarization for Geometry One with Square Aperture Antenna	20
16. Polarization for Geometry One with Variable Sidelobe Levels	20
17. Mean of Chi for Radar Geometry One	22
18. Variance of Chi for Radar Geometry One	22

19. Mean of Gamma for Radar Geometry One	23
20. Variance of Gamma for Radar Geometry One	23
21. Polarization for Geometry Two with the Square Aperture Antenna One Realization.	25
22. Polarization for Geometry Two with Variable Sidelobe Levels One Realization	25
23. Mean of Chi for Radar Geometry Two	25
24. Variance of Chi for Radar Geometry Two	25
25. Mean of Gamma for Radar Geometry Two	25
26. Variance of Gamma for Radar Geometry Two	25

## Clutter Signal Polarization In Bistatic Radar: Effect Of Antenna Sidelobe Clutter

### 1. INTRODUCTION

Clutter signal polarization is of interest in bistatic radar because polarization nulling is being considered as a technique to suppress bistatic clutter 1-3. Clutter suppression can increase the mainbeam signal-to-clutter ratio for low cross section or low altitude targets. Sidelobe clutter reflections are likely to have different polarizations from mainbeam clutter since the incidence and scattering angles upon which the polarization depends will be different. Research to date has not considered the impact of sidelobe clutter on signal polarization. Knowledge of the impact of sidelobe contributions on the polarization of the received clutter signal is important both to predictive clutter nulling algorithms and to polarization measurement radars. This report addresses sidelobe clutter polarization in bistatic radar.

Polarization nulling exploits the fact that a target and clutter have different dielectric properties. The polarization of a reflected wave in bistatic radar depends on the incident and scattering angles and the dielectric properties of the surface. When a signal is reflected from most clutter surfaces its polarization is different from that of the incident wave. The clutter signal can be minimized by adjusting the polarization of the receiving system (assuming a dual polarized receiver) to be orthogonal to the clutter polarization. A target signal would have a

different polarization dependence than the clutter and would not be minimized for that receiver polarization. Therefore the signal-to-clutter ratio would probably be enhanced.

This report develops a formalism for evaluating the mainbeam and mainbeam plus sidelobe clutter signal polarization for an arbitrary radar system. Sidelobe clutter effects are evaluated for two specific radar geometries and two antenna patterns. Uniform clutter conditions are assumed in each case. The results show that there are conditions in which the sidelobes corrupt the mainbeam clutter, yet the conditions are avoidable with proper attention to antenna sidelobe level and radar geometry. Sidelobe contributions should be considered to assure that polarization measurement radars work properly and that polarization cancellation schemes are properly designed.

## 2. POLARIZATION

The polarization of a wave is described by the space-time behavior of its electric field vector  $\vec{E}$ . Figure 1 shows the instantaneous orientation of the electric field of a wave propagating along the positive  $u$  axis towards the reader and can be represented by

$$\vec{E} = E_0 e^{j(\omega t - kx)} \{ \alpha \hat{h} + \beta \hat{v} \} \quad (1)$$

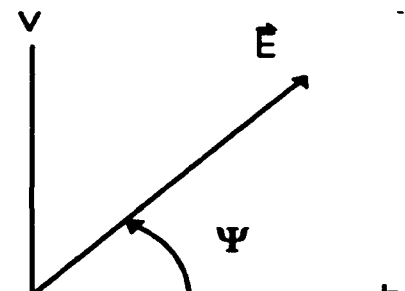


Figure 1 - Electric Field Orientation

where  $\omega$  is the angular frequency,  $\hat{h}$  and  $\hat{v}$  are unit vectors in the  $h$  and  $v$  directions respectively, and  $\alpha$  and  $\beta$  are complex constants that determine wave's polarization and satisfy the relation  $\alpha\alpha^* + \beta\beta^* = 1$ . With  $\alpha = \alpha_m e^{j\alpha_m}$  and  $\beta = \beta_m e^{j\beta_m}$ , the angle  $\Psi$  between  $\hat{h}$  and  $\vec{E}$  can be written as<sup>4</sup>

$$\Psi = \tan^{-1} \left\{ \frac{\beta_m \cos[\omega t - ku + \beta_a]}{\alpha_m \cos[\omega t - ku + \alpha_a]} \right\} \quad (2)$$

Specific values of  $\alpha$  and  $\beta$  yield three distinct polarizations: linear, circular, and elliptical. For linear polarization,  $\alpha_m = \cos \Psi$ ,  $\beta_m = \sin \Psi$ , and  $\alpha_a - \beta_a = 0$ . The magnitude of  $\vec{E}$  varies periodically with time and position but its spatial orientation is fixed. For circular polarization,  $\alpha_m = \beta_m = 1/\sqrt{2}$  and  $\alpha_a - \beta_a = \pm \pi/2$ . In contrast to linear polarization the orientation of the electric field is not fixed and the locus of points spanned by the tip of  $\vec{E}$  is a circle of radius  $E_0/\sqrt{2}$ .  $\vec{E}$  rotates clockwise (when viewed in the direction of propagation) for  $\beta_a - \alpha_a = -\pi/2$  and counterclockwise for  $\beta_a - \alpha_a = \pi/2$ . In both cases the rotation rate is equal to  $\omega$ . CW and CCW rotation are called right-hand and left-hand circular polarization respectively.

Linear and circular polarization are special cases of elliptical polarization. For elliptical polarization  $0 < \alpha_m \neq \beta_m < 1$  and  $\beta_a - \alpha_a \neq 0, \pi/2$ . The behavior of the electric field vector is easier to visualize with the help of the sketch in Figure 2. Now the locus of points spanned by the tip of  $\vec{E}$  is an ellipse. That is,  $|\vec{E}|$  varies as  $\vec{E}$  rotates. Furthermore, the rotation rate is not uniform but varies with the position of  $\vec{E}$ . As with circular polarization, the rotation is CW or CCW depending on the sign of  $\beta_a - \alpha_a$ .

Several methods of describing signal polarization have evolved. Among these are the polarization factor, the Stokes parameters, the Poincaré sphere, and others. The results in this report are presented using a modification of the Poincaré sphere.

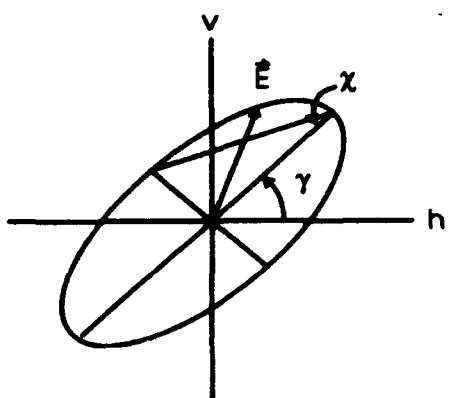


Figure 2 - Elliptically Polarized Field

The Poincaré sphere can be represented in terms of its radius  $s_0$ , the azimuth angle  $2\gamma$  and the latitude angle  $2\chi$ . The radius  $s_0$  is proportional to the power density of the electromagnetic wave and given by

$$s_0 = E_0^2 [\beta_m^2 + \alpha_m^2] \quad (3)$$

Figure 2 shows the inclination angle  $\gamma$ , and eccentricity angle  $\chi$ , of the polarization ellipse. The value of  $\gamma$  is

$$\gamma = \frac{1}{2} \tan^{-1} \left\{ \frac{2\alpha_m \beta_m \cos(\beta_a - \alpha_a)}{\alpha_m^2 - \beta_m^2} \right\} \quad (4)$$

and ranges between  $-\pi/2$  and  $\pi/2$ . The major and minor axes of the ellipse are respectively,

$$M = E_0 \left[ (\alpha_m \cos \gamma + \beta_m \cos(\beta_a - \alpha_a) \sin \gamma)^2 + (\beta_m \sin(\beta_a - \alpha_a) \sin \gamma)^2 \right]^{\frac{1}{2}} \quad (5)$$

and

$$N = E_0 \left[ (\alpha_m \sin \gamma - \beta_m \cos(\beta_a - \alpha_a) \cos \gamma)^2 + (\beta_m \sin(\beta_a - \alpha_a) \cos \gamma)^2 \right]^{\frac{1}{2}} \quad (6)$$

They are used to define the ellipse's eccentricity through the angle  $\chi$ ,

$$\chi = \tan^{-1} \left\{ \frac{N}{M} \right\} = \sin^{-1} \left\{ \frac{2\alpha_m \beta_m \sin(\beta_a - \alpha_a)}{\alpha_m^2 + \beta_m^2} \right\} \quad (7)$$

which ranges between  $-\pi/4$  and  $\pi/4$ . A summary of the values of  $\gamma$ ,  $M$ ,  $N$ , and  $\chi$  is listed in Table 1 for linear and circular polarization.

Table 1 - Parameters for Linear and Circular Polarization

	$\gamma$	$\chi$	M	N
Horizontal	0	0	1	0
Vertical	$\pi/2$	0	1	0
Right Circular	- $\pi/2$ to $\pi/2$	- $\pi/4$	$E_0/\sqrt{2}$	$E_0/\sqrt{2}$
Left Circular	- $\pi/2$ to $\pi/2$	$\pi/4$	$E_0/\sqrt{2}$	$E_0/\sqrt{2}$

A Poincaré sphere is shown in Figure

3. It should be noted that the size of the sphere is proportional to the power density of the wave. A convenient way of representing the polarization of a wave is as follows: First the Poincaré sphere is normalized to make its radius unity. Then a point on the surface of the normalized Poincaré sphere is projected onto the equatorial plane. Such a representation is shown in Figure 4. The coordinates  $\rho$  and  $\theta$  of a point in this new representation are

$$\rho = \cos(2\chi)$$

and

$$(8)$$

$$\theta = 2\gamma.$$

All points that lie on the circle  $\rho = 1$

represent linear polarization. Horizontal and vertical polarization further require that

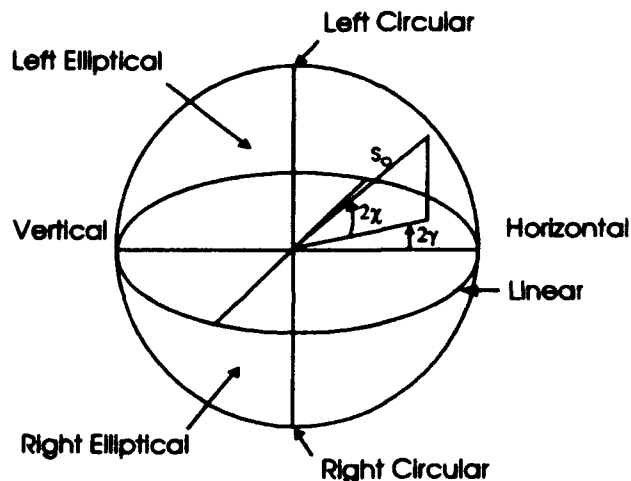


Figure 3 - Poincaré Sphere

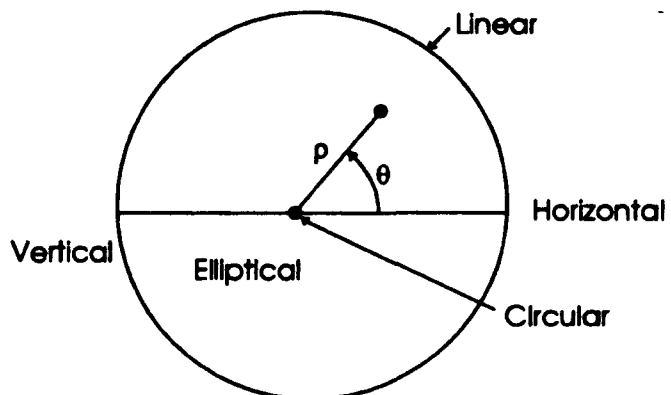


Figure 4 - Projection of Poincaré Sphere onto Equatorial Plane

$\theta = 0$  or  $\pi$  respectively. Circular polarization is represented by a point in the center. Note that the representation loses the information on the left and right hand sense of polarization. This representation will be used to show the effect of sidelobe clutter on polarization of the clutter signal.

### 3. CLUTTER CROSS SECTION

Figure 5 shows the bistatic scattering geometry and defines the angle of incidence  $\theta_i$ , the scattering angle  $\theta_s$ , the azimuth angle  $\varphi_s$ .  $\bar{E}$  and  $\bar{E}'$  are the electric fields of the incident and reflected wave respectively. The reflecting rough surface is assumed to be made up of many randomly oriented facets each large compared to the wavelength  $\lambda$ . When the incident wave strikes the rough surface, only those facets whose normals lie in the plane defined by the unit vectors  $\hat{u}$  and  $\hat{u}'$  and bisect the bistatic angle contribute to the energy scattered in the  $\hat{u}'$  direction.

The complete description of the wave  $\bar{E}'$  scattered from the illuminated patch is found from the surface's scattering matrix  $\mathbf{S}$ . In particular,

$$\begin{pmatrix} E'_h \\ E'_v \end{pmatrix} = \frac{e^{-j\theta_i}}{\sqrt{4\pi u'^2}} \begin{pmatrix} S_{hh} & S_{hv} \\ S_{vh} & S_{vv} \end{pmatrix} \begin{pmatrix} E_h \\ E_v \end{pmatrix} \quad (9)$$

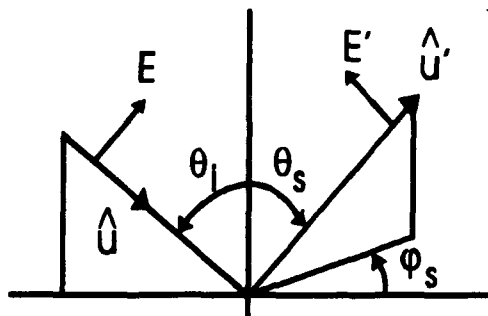


Figure 5 - Bistatic Scattering Geometry

where the subscripts  $h$  and  $v$  indicate horizontal and vertical and the primed and unprimed quantities indicate reflected and incident values respectively. The elements of the scattering matrix are related to those of the radar cross section matrix so that

$$S_{pq} = |S_{pq}| \exp[j \arg(S_{pq})] = \sqrt{\sigma_{pq}} \exp[j \arg(S_{pq})]. \quad (10)$$

Thus  $\mathbf{S}$  or  $\sigma$  and  $\arg(S_{pq})$  completely determine the magnitude, phase, and polarization of  $E'$ . For a rough surface, the  $S_{pq}$  are random quantities that depend on the roughness and dielectric constant of the surface and on  $\theta_i$ ,  $\theta_s$ , and  $\varphi_s$ . The cross sections  $\sigma_{pq}$  are the observed cross sections for that realization and not an average cross section. The normalized (but not averaged) clutter cross section  $\sigma^c_{pq}$  is

$$\sigma'_{pq} = \frac{\sigma_p}{A} \quad (11)$$

where  $A$  is the size of the clutter cell under consideration. The mean value of  $\sigma_{pq}^0$ ,  $\bar{\sigma}_{pq}^0$  is the reflectivity of the surface and is the quantity usually used in the radar range equation.

It is convenient to set  $s_{apq} = \arg(S_{pq})$  and to write the element scattering amplitudes as

$$S_{pq} = \sqrt{A} r_{pq} s_{mpq} \exp[j s_{apq}] \quad (12)$$

The deterministic coefficients  $r_{pq}$  are obtained from the Fresnel reflection coefficients (discussed below) and depend only on the surface's relative dielectric constant  $\epsilon_r$ , and the angles  $\theta_i$ ,  $\theta_s$ , and  $\varphi_s$ .  $s_{mpq} = \sqrt{\sigma_{pq}^0}$  is a random variable whose mean is  $\sqrt{\bar{\sigma}_{pq}^0}$ . When multiplied by  $\sqrt{A}$  it gives the effective amplitude of the clutter in a particular resolution cell. The probability density function  $p(s_{mpq})$  that describes the statistics of the clutter is Rayleigh for many surfaces and can be represented by<sup>5</sup>

$$p(s_{mpq}) = \frac{s_{mpq}}{\langle s_{mpq}^2 \rangle} \exp\left[\frac{-s_{mpq}^2}{2\langle s_{mpq}^2 \rangle}\right] \quad (13)$$

where the angular brackets indicate the mean value of the enclosed quantity, hence  $\langle s_{mpq}^2 \rangle = \bar{\sigma}_{pq}^0$ . The  $s_{apq}$  are also random, independent of  $s_{mpq}$ , and uniformly distributed over the interval 0 to  $2\pi$ .

As long as the scattering facets are large compared to a wavelength, the polarization of  $\vec{E}'$  depends only on the geometry of the reflection process and not on the specific nature of the rough surface<sup>1</sup>. Thus the representation of the rough surface in the form of the random variables  $s_{mpq}$  and  $s_{apq}$  is polarization independent. So for a particular scattering facet,  $S$

reduces from matrix form to the random variable  $s_m \exp(jS_a)$ . The scattering matrix elements can be written as

$$S_{pq} = \sqrt{A} r_{pq} s_m \exp[jS_a] \quad (14)$$

and the scattering matrix as

$$[S] = \sqrt{A} s_m \exp[jS_a] \begin{pmatrix} r_{hh} & r_{hv} \\ r_{vh} & r_{vv} \end{pmatrix}. \quad (15)$$

The coefficients  $r_{pq}$  are

$$\begin{aligned} r_{hh} &= R_h \cos \beta_1 \cos \beta_2 + R_v \sin \beta_1 \sin \beta_2, \\ r_{vh} &= -R_h \cos \beta_1 \sin \beta_2 + R_v \sin \beta_1 \cos \beta_2, \\ r_{vv} &= R_h \sin \beta_1 \sin \beta_2 + R_v \cos \beta_1 \cos \beta_2, \end{aligned} \quad (16)$$

and

$$r_{hv} = -R_h \sin \beta_1 \cos \beta_2 + R_v \cos \beta_1 \sin \beta_2$$

where  $R_h$  and  $R_v$  are the Fresnel reflection coefficients of the tilted reflecting facets. They are

$$R_v = \frac{\epsilon_r \cos \theta - (\epsilon_r - \sin^2 \theta)^{1/2}}{\epsilon_r \cos \theta + (\epsilon_r - \sin^2 \theta)^{1/2}} \quad (17)$$

and

$$R_h = \frac{\cos \theta - (\epsilon_r - \sin^2 \theta)^{1/2}}{\cos \theta + (\epsilon_r - \sin^2 \theta)^{1/2}}. \quad (18)$$

where  $\epsilon_r$  is the complex relative dielectric constant of the reflecting surface. The angles  $\theta$ ,  $\beta_1$ , and  $\beta_2$  describe the tilt of the specular reflecting surfaces in the reference coordinate system and are related to  $\theta_i$ ,  $\theta_s$ , and  $\varphi_s$  by the expressions

$$\cos 2\theta = \cos \theta_i \cos \theta_s - \sin \theta_i \sin \theta_s \cos \varphi_s,$$

$$\sin \beta_1 = \sin \varphi_s \sin \theta_s / \sin 2\theta,$$

and

(19)

$$\sin \beta_2 = \sin \theta_i \sin \varphi_s / \sin 2\theta.$$

As an example, the co- and cross-polarized components of the reflected field from terrain characterized by  $\epsilon_r = 4 + j0.45$  (typical for a forest canopy) for a vertically polarized incident wave are plotted in Figures 6 and 7. It is apparent that the polarization of the reflected wave varies with the scattering and azimuth angles. In fact, the co-polarized component of the reflected wave is often suppressed, its energy having been converted into the orthogonal polarization by the bistatic reflection process. The location of the null in the co-polarized pattern depends only on the angle geometry and the dielectric constant of the reflecting surface.

Depending on the configuration of the radar system, the incident and scattering angles in the sidelobe region can vary tremendously. This causes the magnitude of the reflected vertical and horizontal components to vary substantially as seen in Figures 6 and 7. The variation of these components indicates that the polarization of the signals reflected from the sidelobes, if sufficiently large, can change the polarization of the received clutter signal.

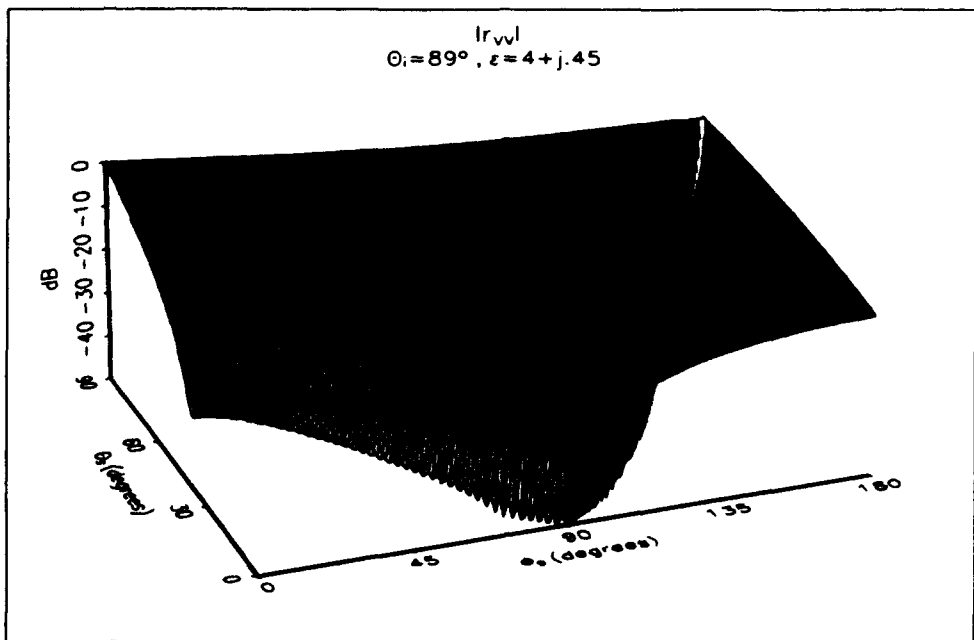


Figure 6 - Co-Polarized Component of the Scattered Electric Field

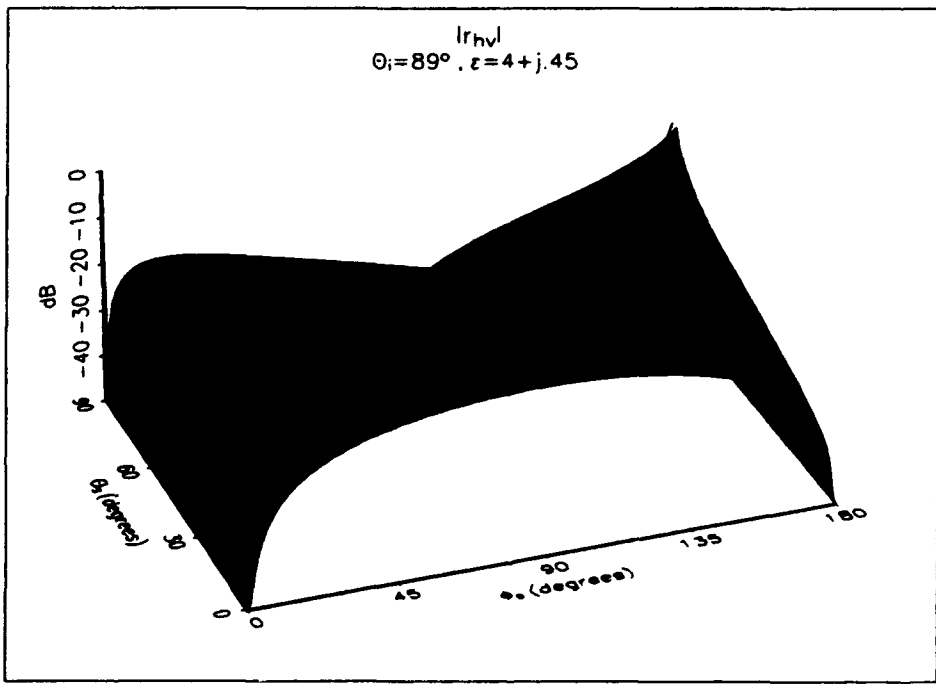


Figure 7 - Cross-Polarized Component of the Scattered Electric Field

#### 4. RADAR GEOMETRIES

The bistatic radar geometry under consideration is shown in Figure 8. The radar transmitter and receiver are located at the foci of an ellipse in a local (primed) coordinate system. The semi-major and semi-minor axes of the ellipse are  $a$  and  $b$  respectively and the distance between the foci is  $2x_0$ . The total range delay from the transmitter to the clutter patch to the receiver is  $L$ . Now  $L = 2a$  and  $b = \sqrt{a^2 - x_0^2}$ .  $H$  is the average of the transmitter and receiver heights. The surfaces of constant range delay are concentric ellipsoids with common foci and satisfy the relation

$$\frac{x'^2}{a^2} + \frac{y'^2}{b^2} + \frac{z'^2}{b^2} = 1 \quad (20)$$

The clutter contributions arise from the intersections of these ellipsoids with the earth's surface. The intersections are ellipses only when the transmitter and receiver are at the same height. When the

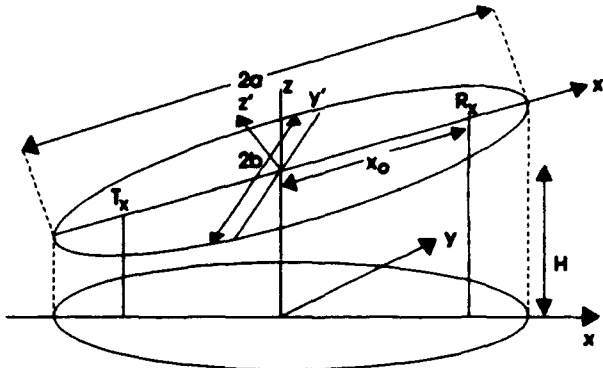


Figure 8 - Bistatic Radar Geometry

two are not at the same height, a coordinate transformation must be applied to Eq. (20) to transform from the local coordinates to the global system coordinates before the intersections with the ground can be found. The transformations that take the primed coordinates into the unprimed system by a rotation about the  $y'$  axis are

$$\begin{aligned} x' &= x \cos \theta - z \sin \theta \\ y' &= y \\ z' &= x \sin \theta + z \cos \theta \end{aligned} \quad (21)$$

$$\theta = \sin^{-1} \left( \frac{H_R - H_T}{2x_0} \right)$$

where  $H_T$  and  $H_R$  are the heights of the transmitter and receiver respectively.

Two independent radar geometries were selected to examine the impact of sidelobe contributions on clutter signal polarization. Two antenna patterns were used in each case to determine a sidelobe level at which sidelobe polarization contributions become significant. Geometry No. 1 represents an existing clutter measurement system. Its transmitter and receiver heights are relatively small and nearly equal. Configuration No. 2 uses a ground based transmitter and an airborne receiver. This produces incident and scattering angles that cause signal depolarization.

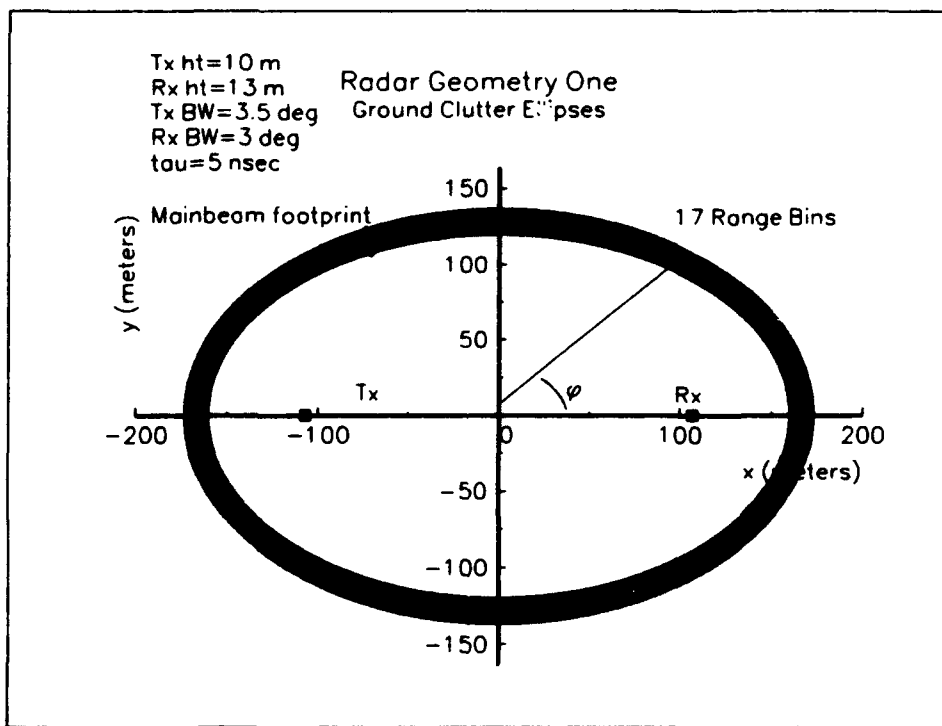


Figure 9 - Radar Geometry One. Approximates experimental clutter measurement setup.

Radar Geometry One is shown in Figure 9. The geometry is based on an experimental clutter measurement system located at Rome Laboratory's Ipswich facility. The baseline range is 214 m. The antennas are boresighted at a point with the coordinates (x = -72 m, y

= 115 m) with respect to the center of the transmitter receiver baseline. A transmit beamwidth of  $3.5^\circ$ , receive beamwidth of  $3^\circ$  and a pulsedwidth of 5 ns produce 17 range bins in the mainbeam intersections. The nearly elliptical band represents the overlap region of the transmitting and receiving antenna footprints for the selected conditions. Within this band are a number of constant range delay rings. (There are too many to resolve in the figure.) The spacing between rings of constant range delay depends on the width  $\tau$  of the transmitted pulse. The cluster of four diamonds in the upper left quadrant of the figure show the four corners of the mainbeam footprint. The shortest and longest range delays that fit within the antenna pattern footprint are shown in Figure 9.

A point on a constant range ring is located by the angle  $\phi$  as shown in Figure 9. Once  $\phi$  is specified,  $\theta_i$ ,  $\theta_s$ ,  $\phi_s$ , and  $\beta$  can be found and the Fresnel reflection coefficients computed.

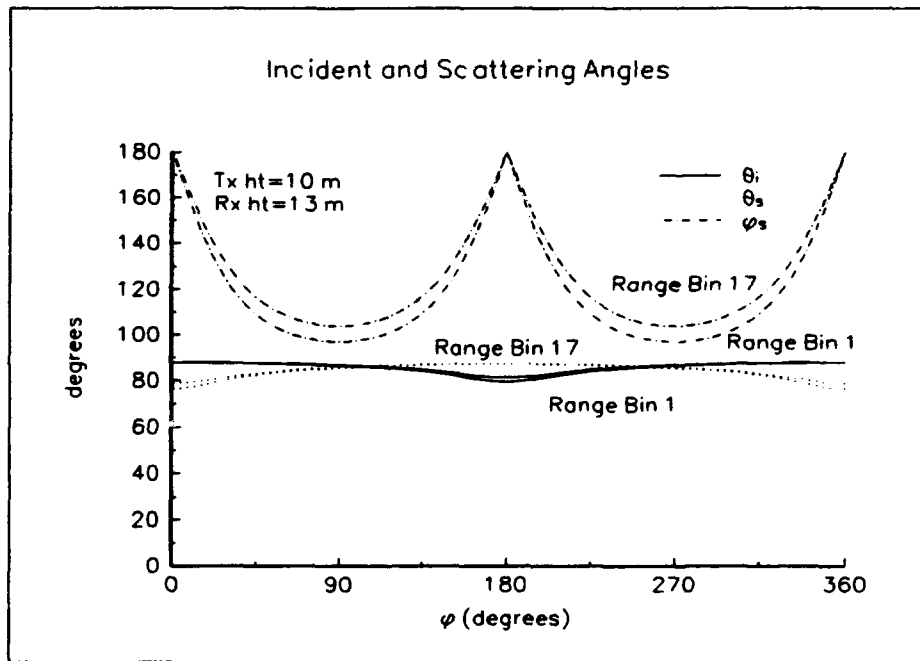


Figure 10 - Incidence and Scattering Angles for Geometry One

Figure 10 shows the incident and scattering elevation angles and the scattering azimuth angle as a function of the parameter  $\phi$ , the angle from the x axis to the point under

consideration, as shown in Figure 9. It is apparent that the incident and scattering elevation angles are always close to  $90^\circ$  due to the relatively low receiver and transmitter heights. The azimuth angle is the only quantity that varies significantly.

Radar Geometry Two is shown in Figure 11. The baseline range is 10 km and the mainbeam footprint is located at ( $x = -7000$  m,  $y = 6500$  m) relative to the origin at the center of the transmitter-receiver baseline. A transmit beamwidth of  $3^\circ$ , receiver beamwidth of  $2.5^\circ$ , and receiver pulsedwidth of  $1 \mu\text{sec}$  produce 8 range bins in this geometry.

Figure 12 shows the incidence and scattering angles as a function of  $\varphi$  for this geometry. Since the receiver height is 9 km, both  $\varphi$  and  $\theta_s$  vary significantly around the sidelobe region.

It is possible for certain segments of the constant range delay rings to be beyond the horizon of the transmitter, the receiver, or both. Therefore, the slant ranges from the transmitter

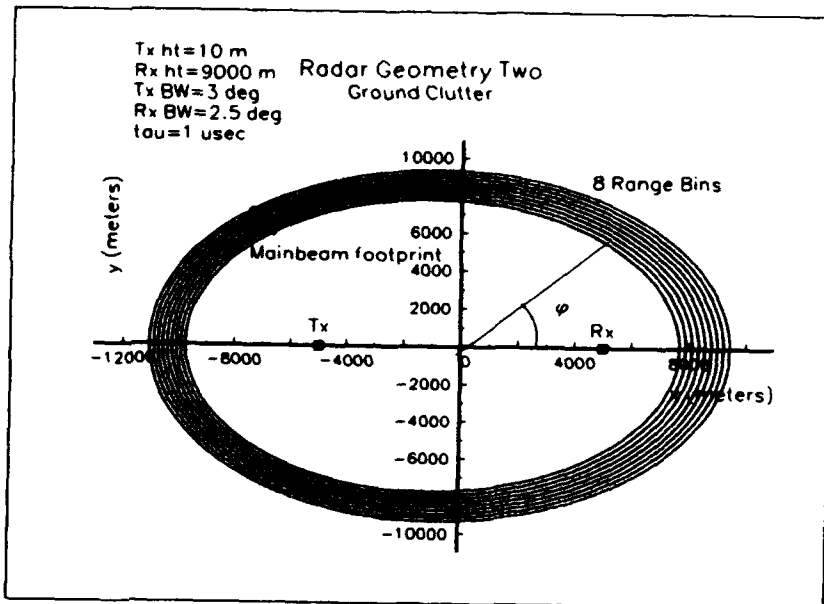


Figure 11 - Radar Geometry Two

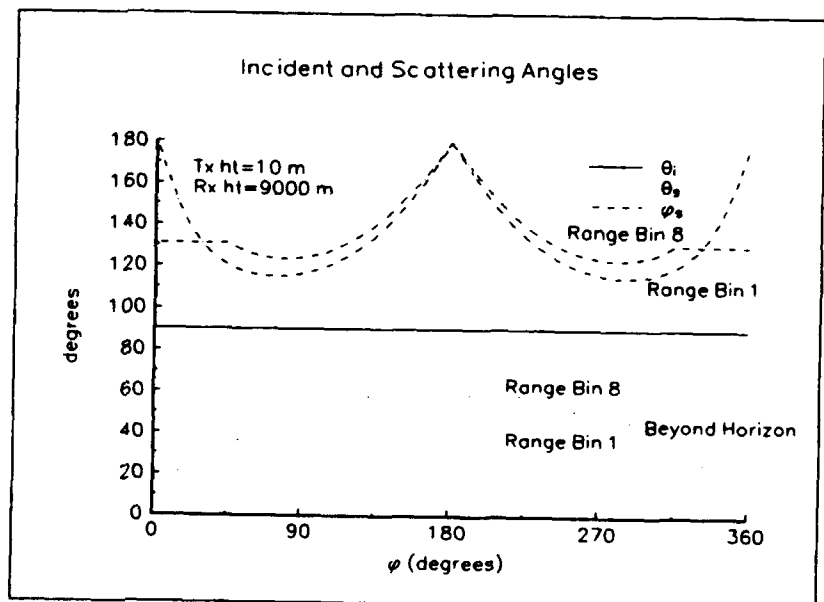


Figure 12 - Incidence and Scattering Angles for Geometry Two

and receiver to the clutter source must be calculated as a function of  $\varphi$  to make certain that clutter can in fact originate from a given point. The criterion is that the slant ranges (in nautical miles) must be less than  $1.23\sqrt{H_i}$  where  $H_i$  is the transmitter or receiver height (in feet).

The field incident at the mainbeam clutter patch is

$$\bar{E} = \left( \frac{P_T G_T 2z_0}{4\pi u^2} \right)^{1/2} [\alpha \hat{h} + \beta \hat{v}] e^{j(\omega t - k u)} \quad (22)$$

where  $P_T$  is the peak transmitter power,  $G_T$  is the gain of the transmitting antenna, and  $z_0$  is the free space impedance. To make the calculations that follow clearer,  $\alpha$  is set equal to zero so that the incident wave is vertically polarized. Then the wave scattered from the clutter patch can be represented as

$$\bar{E}'_{MB} = \left( \frac{P_T G_T 2z_0}{4\pi u^2 u'^2} \right)^{1/2} e^{j(\omega t - k(u+u'))} \sqrt{A} s_m e^{j\varphi_m} \{ r_{h'} \hat{h} + r_{v'} \hat{v} \} \quad (23)$$

It is apparent from Eq. (23) that the polarization of the scattered wave at the receiving antenna depends only on  $r_{h'}$  and  $r_{v'}$  where the quantities are evaluated at the mainbeam position  $\varphi = \varphi_{MB}$ .

The sidelobe clutter originates from the quasi elliptical annulus between two adjacent constant range delay rings. The annulus is divided into a number of angular increments indexed by  $\varphi$ . The total sidelobe clutter is obtained by summing the incremental contributions throughout the sidelobe region. The expression analogous to Eq. (23) for the sidelobe clutter is

$$\bar{E}'_{SL} = \sum_0^N \left( \frac{P_T G_{SL} 2z_0}{4\pi u_n^2 u'_n^2} \right)^{1/2} e^{j(\omega t - k(u_n + u'_n))} \sqrt{A_n} s_{mn} e^{j\varphi_m} \{ r_{h'm} \hat{h} + r_{v'm} \hat{v} \} \quad (24)$$

where  $G_{TSL}$  is the sidelobe gain of the transmitting antenna and the subscript n serves to explicitly indicate that  $A_n, S_n, S_a, r_n$ , and  $r_a$  vary as  $\phi$  sweeps around. Also,  $G_{TSL}$  depends on  $\phi$ , the pattern factor being evaluated for each point in the sidelobe area.

The voltage produced at the terminals of a receiving antenna in response to an incident wave is  $V = \vec{P} \cdot \vec{E}'$  where  $\vec{P}$  is the polarization of the receiving antenna. In this analysis two antennas are used to receive the vertical and horizontal components of the signal. Thus

$$\vec{P}_h = \left( \frac{G_R \lambda^2}{4\pi} \right)^{1/2} \hat{h} \quad \vec{P}_v = \left( \frac{G_R \lambda^2}{4\pi} \right)^{1/2} \hat{v} \quad (25)$$

where  $G_R$  is the gain of the receiving antenna in the direction of the clutter source. The polarization of the received signal is found by using Eq. (25) to sum the vertical and horizontal components of the mainbeam and sidelobe signals in Eqs. (23) and (24). The polarization of the total signal is then obtained from the relative amplitude and phase of the two components.

## 5. ANTENNA PATTERNS

Two antenna patterns were selected, the first to assess the performance of a typical antenna and the second to determine the sidelobe level at which the signal polarization will vary from its mainbeam value. The first pattern, shown in Figure 13, is representative of a square aperture antenna. The pattern factor is given by the equation,<sup>7-8</sup>

$$f = \frac{\sin^2\left(\frac{\pi w}{\lambda} \cos(\Phi) \sin(\theta)\right) \sin^2\left(\frac{\pi w}{\lambda} \sin(\Phi)\right)}{\left(\frac{\pi w}{\lambda} \cos(\Phi) \sin(\theta)\right)^2 \left(\frac{\pi w}{\lambda} \sin(\Phi)\right)^2} \quad (26)$$

where  $\theta$  is the azimuth angle, measured from antenna boresight and  $\Phi$  is the elevation angle, measured from boresight,  $w$  is the height and width of the aperture, and  $\lambda$  is the wavelength. This pattern was used for both the transmitter and the receiver. The transmitter and receiver beamwidths can be specified and the gain approximated by

$$G = \frac{4\pi}{\Theta_B \Phi_B}. \quad (27)$$

where  $\Theta_B$  and  $\Phi_B$  are the 3 dB azimuth and elevation plane beamwidths respectively. In the clutter calculations, the sidelobe level of the pattern outside the antenna's forward hemisphere was set to the level at the edges of the hemisphere.

The second antenna pattern is a simple approximation of a circular aperture. The entire sidelobe region is set at a constant gain below that of the mainbeam. Figure 14 shows this antenna pattern. The gain of the sidelobes relative to that of the mainbeam is stepped through a series of different values. This technique is used to determine at which point the sidelobe clutter corrupts the mainbeam polarization. Even though this is not a realistic antenna pattern, the combination of the sidelobe level, azimuth angle range and the elevation angle range can be compared to the integrated sidelobes of a real antenna pattern and used to estimate if there will be polarization corruption using the real antenna.

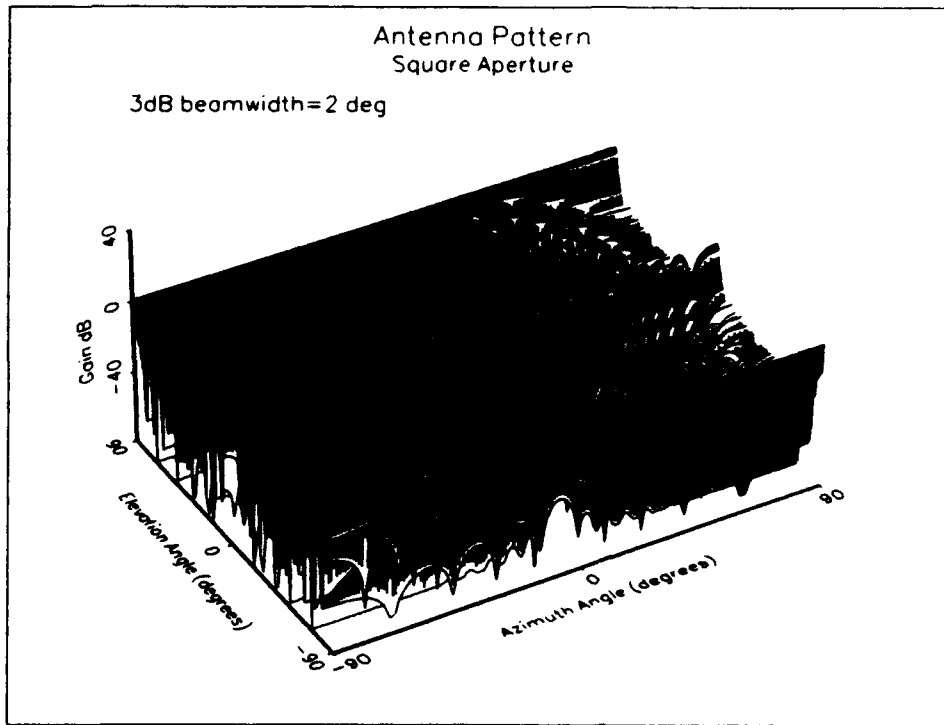


Figure 13 - Square Aperture Antenna Pattern

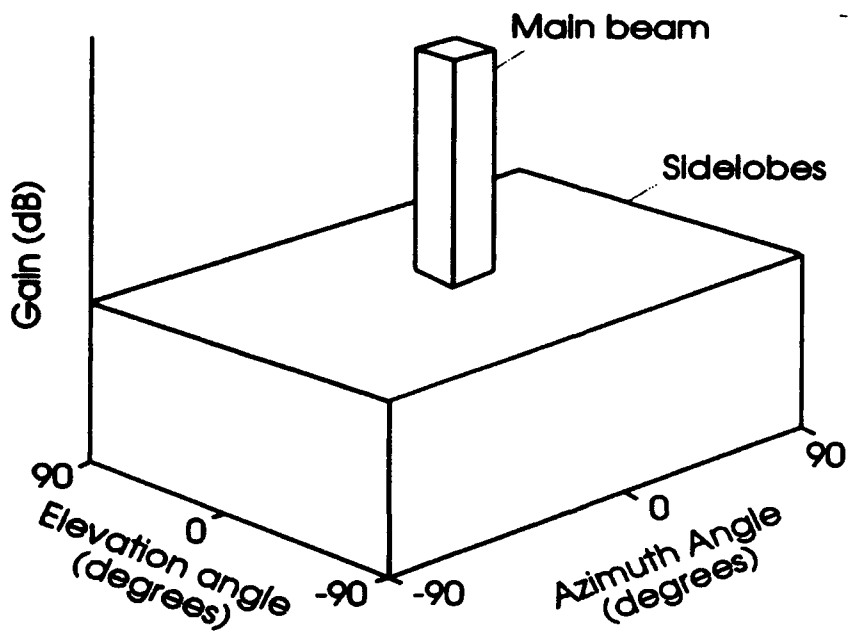


Figure 14 - Variable Sidelobe Level Antenna Pattern

## 6. CALCULATIONS AND RESULTS

In the calculations, the transmitter polarization was always vertical and the operating frequency was 3 GHz. The clutter is homogeneous in both the mainbeam and sidelobe regions with  $\epsilon_r = 4 + j0.45$  (surface dielectric constant), and  $\bar{\sigma}_0 = -41$  dB (normalized clutter cross section). These parameters are representative of forested terrain. In the calculations, it is assumed that  $\bar{\sigma}_0$  does not change as  $\phi$  sweeps around a clutter annulus. However, every range bin and angular segment sample of the clutter annulus is a different realization of the two random quantities  $s_m$  and  $s_a$ . Because of this, two sets of random numbers representing samples for  $s_m$  with a Rayleigh probability density function (Eq. 13) and samples for  $s_a$  with a uniform probability density function were generated. New samples for  $s_m$  and  $s_a$  are used every time  $\phi$  is indexed to a new clutter segment or the calculations done for another range bin.

Figure 15 shows the polarization of the mainbeam clutter signal and the mainbeam plus sidelobe signal for all 17 range bins in Geometry No. 1. The square aperture antenna was used in this case. The dots and triangles cannot be resolved independently because they

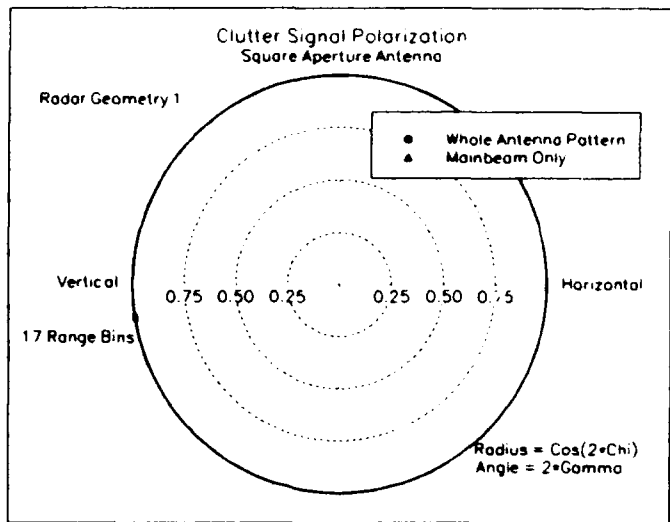


Figure 15 - Polarization for Geometry One with Square Aperture Antenna

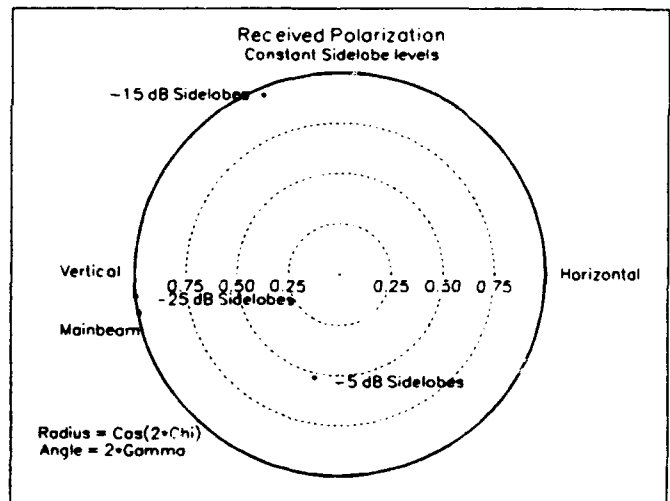


Figure 16 - Polarization for Geometry One with Variable Sidelobe Levels

overlay one another. Note that for vertical incidence the reflection is near vertical. It is apparent that the impact of the sidelobes on the mainbeam polarization is minimal in this case.

Figure 16 shows results for Geometry No. 1 for the variable sidelobe level antenna pattern. In this case, only the polarization for one range bin is displayed. The mainbeam polarization point is identical the point found using the square aperture antenna. The sidelobe gain was stepped from -55 dB to -5 dB in 10 dB increments. The points labeled -25 dB, -15 dB, and -5 dB clearly show mainbeam clutter plus sidelobe clutter polarizations different from the mainbeam clutter alone. (These numbers are the sidelobe gain relative to the mainbeam gain.) This is because the sidelobe clutter is of the same magnitude as the mainbeam clutter. The points for sidelobe levels -35 dB, -45 dB and -55 dB below the mainbeam are also on the plot but the polarization in these cases coincides with the mainbeam polarization and the points are not apparent. Thus for these sidelobe levels, the sidelobe clutter is small compared to the mainbeam clutter.

It should be noted that a different set of random numbers for  $s_m$  and  $s_a$  would result in different polarizations from those shown in Figure 16. If for a particular realization of the random quantities  $s_m$  and  $s_a$  the sidelobe clutter is large then the effect on the mainbeam clutter polarization will be pronounced. Another realization might produce a small sidelobe contribution to the total clutter and therefore not affect the mainbeam clutter polarization. Because of this, the results that follow are presented in terms of the average values of  $\gamma$  and  $\chi$  for many sets of random numbers applied to the geometry under investigation.

The equations for the mean and variance are,

$$E(\gamma) = \frac{1}{N} \sum_i \gamma_i, \quad (28)$$

$$(\gamma) = \frac{1}{N} \sum_i \gamma_i^2 - E(\gamma)^2, \quad (29)$$

$$E(\chi) = \frac{1}{N} \sum_i \chi_i, \quad (30)$$

$$(\chi) = \frac{1}{N} \sum_i \chi_i^2 - E(\chi)^2 \quad (31)$$

where  $E$  indicates the expected value or mean, and  $V$  the variance.

A 500 trial Monte Carlo run was done for each integer sidelobe level from -30 dB to -10 dB (using the variable sidelobe level antenna pattern). Both antenna geometries were used. The first range bin in each was used for calculations. The mean and variance of both  $\gamma$  and  $\chi$  for the mainbeam alone and the mainbeam plus sidelobe clutter signals were calculated. When these cases are plotted together as a function of sidelobe level a meaningful estimate of the required sidelobe level to avoid polarization corruption can be made. These plots are in the next section.

Figure 17 shows the mean value of chi for Radar Geometry No. 1. The mainbeam value varies less than 0.1 degree as the sidelobe level is increased. The mean of chi for the mainbeam plus sidelobe does vary as the sidelobe level is increased but not more than 1 degree. Figure 18 shows the variance of chi as a function of sidelobe level. As expected, the variance increases with sidelobe level, although only by 4 degrees at the -10 dB sidelobe level.

Figure 19 shows the mean value of gamma for Radar Geometry No. 1 and Figure 20 shows the variance of gamma. It is clear from these plots that the mean value of gamma for the mainbeam plus sidelobe clutter tracks that of the mainbeam only up to a sidelobe value of -25 dB. At higher sidelobe levels the value of gamma for the sum deviates significantly, in both mean and variance, from that of the mainbeam only.

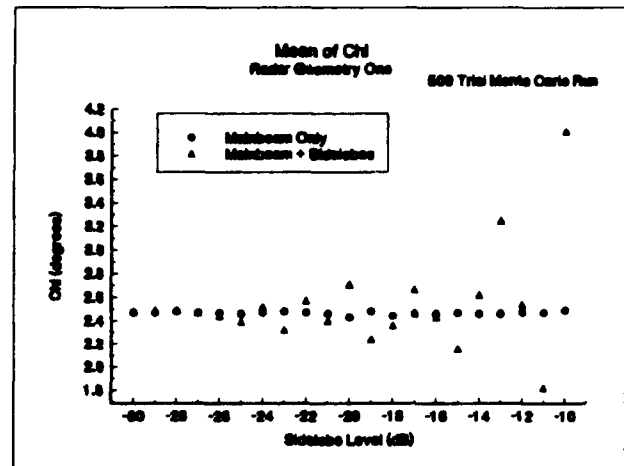


Figure 17 - Mean of Chi for Radar Geometry One

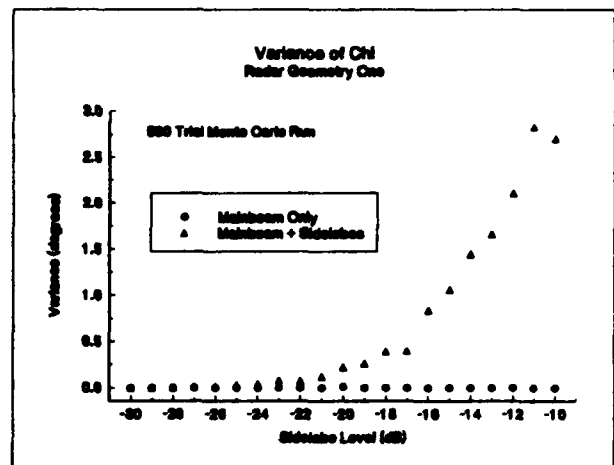


Figure 18 - Variance of Chi for Radar Geometry One

Figure 21 shows the polarization states for the received signals for the 8 range bins in the second radar configuration. In this case there is a somewhat greater variation between range bins because the angles from one to the other are slightly different. This combined with the independent samples for the eight sidelobe calculations produce the cluster of points shown in the figure.

There is strong depolarization for this geometry; the vertically polarized incident energy is reflected into an elliptically polarized wave. Examination of Figure 15 in conjunction with Figure 7 makes it clear why there is change from the mainbeam values when the sidelobes are added in. The mainbeam lies in a null on Figure 7. A slight variation in scattering angles will cause the reflected wave to have a vertically polarized component that when added to the mainbeam value will change the signal polarization.

Figure 22 shows the results for the first range bin in Radar Geometry No. 2 and the stepped sidelobe level antenna pattern. There is significant variation for the -25 dB, -15 dB, and -5 dB levels.

The result of the Monte Carlo runs for Radar Geometry No. 2 are shown in Figures 23 through 25. The behavior of the polarization as a function of sidelobe level is quantified in these plots. Figure 23 shows the mean of chi. The sidelobe contributions affect the mean value of chi when the sidelobe level is above a value of -20 dB. The change is less than 6

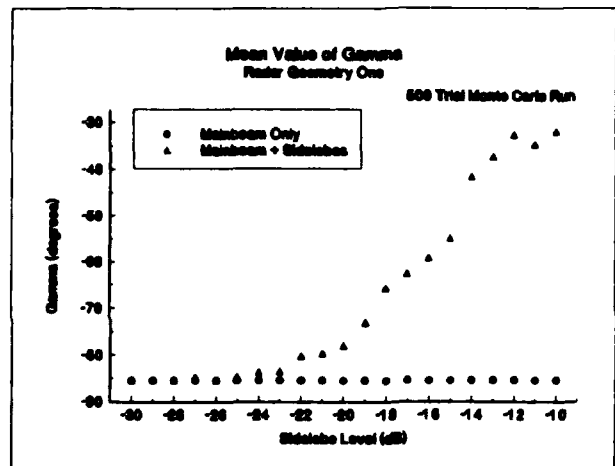


Figure 19 - Mean Value of Gamma for Radar Geometry One

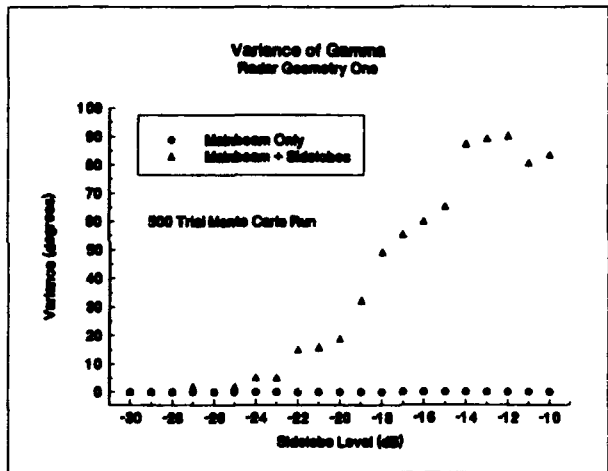


Figure 20 - Variance of Gamma for Radar Geometry One

degrees. The variance of chi, shown in Figure 24, is also relatively small, reaching 3.5 degrees at a sidelobe level of -10 dB. Figure 25 shows the mean value of gamma for Radar Geometry No. 2 as a function of sidelobe level. The mainbeam plus sidelobe value is very close to the mainbeam-only value for sidelobe levels of -18 dB and below. The mean deviates by 12 degrees at most for this case, in contrast to Radar Geometry No. 1. The variance of gamma, shown in Figure 26, is also smaller for this radar geometry, 19 degrees at -10 dB sidelobe level. Figures 23 through 26 all show gamma and chi to be close to the mainbeam-only value for sidelobe levels below -20 dB.

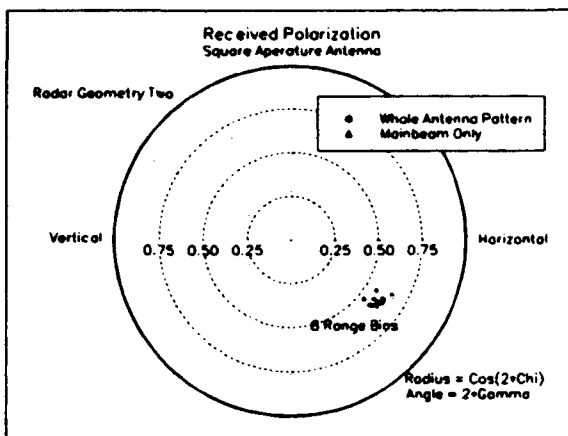


Figure 21 - Radar Geometry Two with the Square Aperture Antenna. One Realization.

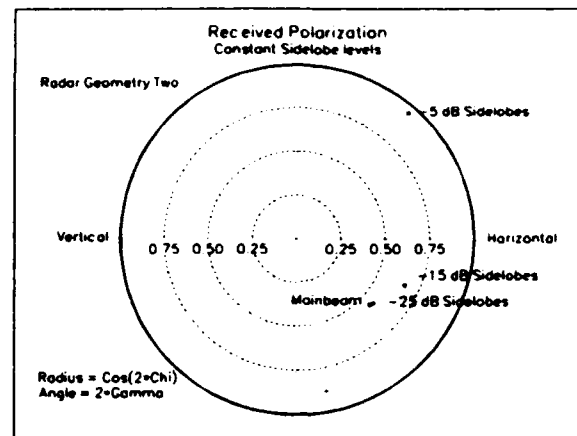


Figure 22 - Polarization for Geometry Two with Variable Sidelobe Levels. One Realization.

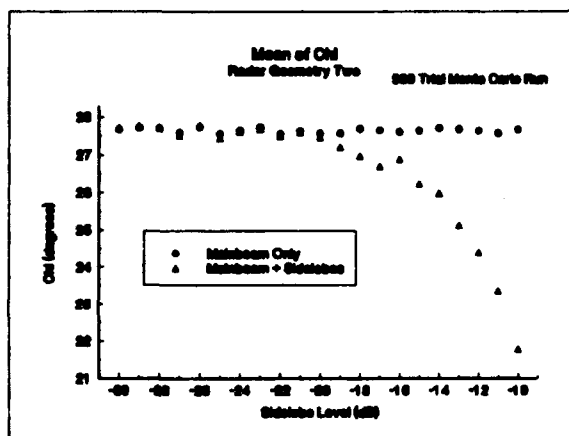


Figure 23 - Mean of Chi for Radar Geometry Two

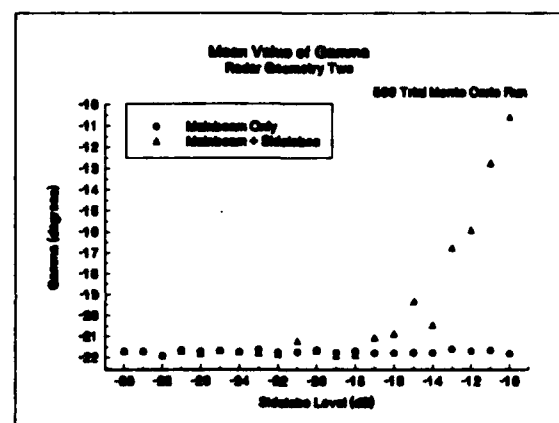


Figure 25 - Mean of Gamma for Radar Geometry Two

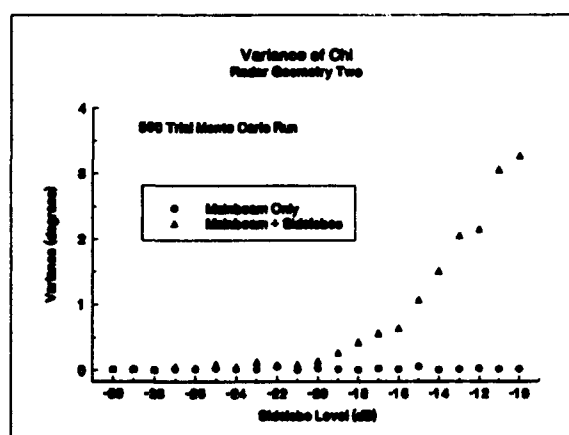


Figure 24 - Variance of Chi for Radar Geometry Two

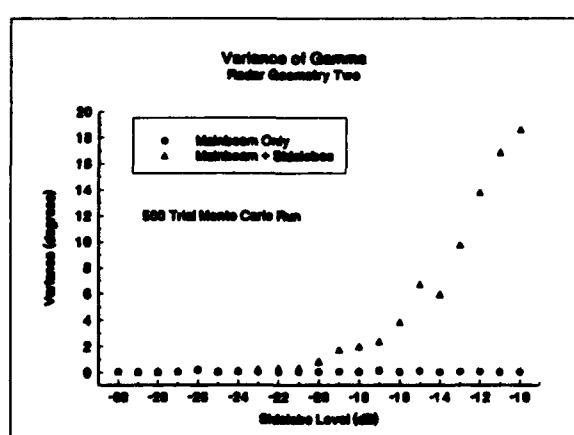


Figure 26 - Variance of Gamma for Radar Geometry Two

## 7. CONCLUSIONS

Under certain conditions, contributions from sidelobe clutter can significantly impact the polarization of the received signal. The effect can be mitigated with low enough sidelobes. If the radar system antennas have reasonably low sidelobes, no special considerations need be made in clutter cancellation schemes or in polarization measurement radars.

The results support some general conclusions. First note that for both radar geometries the difference between the mainbeam only value and the mainbeam plus sidelobe value of gamma is substantially larger than that of chi. The variance of gamma is also larger than that of chi as the sidelobe level is increased. Gamma represents the tilt of the scattered wave and chi the ellipticity. This indicates that the scattering process changes the tilt of the scattered wave more than the ellipticity. It would be interesting to see how the dielectric constant and mean clutter cross section influence this result.

Comparing the two radar geometries, we see that chi varies significantly more for Radar Geometry No. 2 than for Radar Geometry No. 1. This is due to the position of the mainbeam. The mainbeam reflection angles lie near a polarization null caused by the Fresnel reflection coefficient. This causes the received signal polarization to be elliptical. When the sidelobe components are added in, they pull the polarization back toward vertical.

This analysis was only for homogenous clutter and two specific cases. Other cases could be analyzed to determine the impact of non-homogenous clutter and large specular reflectors in the sidelobe region. The impact of the sidelobe effects on clutter polarization nulling performance of a radar depends on the specific system. On one hand, nulling all the clutter from any source should always improve the signal-to-clutter ratio. On the other hand, the target polarization might be the same as the polarization of some of the sidelobe clutter and optimum improvement would not be obtained because the target would also be nulled. As long as the sidelobe levels of a radar system are below about -20 to -25 dB, sidelobe clutter will not affect the polarization of the signal significantly.

## References

1. Papa, Robert J., Lennon, J. F., and Taylor, R. L. (1985) *A Technique for Terrain Clutter Suppression on Bistatic Radars with Polarization Diversity*, RADC-TR-85-200, ADB 100814.
2. Poirier, J. L. (1989) *Clutter Polarization Nulling in Bistatic Radar*, RADC-TR-89-271, ADB 147016L.
3. Poirier, J. L. (1989) *Depolarization in Bistatic Scattering: Effect of Antenna Polarization on System Performance*, RADC-TR-89-272, ADB 147009L.
4. Beckman, P. (1968) *The Depolarization of Electromagnetic Waves*, Golem Press, Boulder, CO.
5. Skolnik, Merrill, Editor (1990) *Radar Handbook*, McGraw-Hill, NY, 2nd edition.
6. Lennon, John F., Papa, Robert S., and Taylor, Richard L. (1986) *A General Bistatic Model of Scattering from Rough Surfaces With Application to the Analysis of Terrain Enhanced Jamming*, RADC-TR-86-15, ADB 103520L.
7. Stutzman, Warren L., and Thiele, Gary A. (1981) *Antenna Theory and Design*, John Wiley & Sons, NY.
8. Rudge, A. W., Milne, K., Olver, A. D., Knight, P. (editors) (1986) *The Handbook of Antenna Design*, Vol. 1 & 2, IEE, London.

***MISSION  
OF  
ROME LABORATORY***

**Mission.** The mission of Rome Laboratory is to advance the science and technologies of command, control, communications and intelligence and to transition them into systems to meet customer needs. To achieve this, Rome Lab:

- a. Conducts vigorous research, development and test programs in all applicable technologies;
- b. Transitions technology to current and future systems to improve operational capability, readiness, and supportability;
- c. Provides a full range of technical support to Air Force Materiel Command product centers and other Air Force organizations;
- d. Promotes transfer of technology to the private sector;
- e. Maintains leading edge technological expertise in the areas of surveillance, communications, command and control, intelligence, reliability science, electro-magnetic technology, photonics, signal processing, and computational science.

The thrust areas of technical competence include: Surveillance, Communications, Command and Control, Intelligence, Signal Processing, Computer Science and Technology, Electromagnetic Technology, Photonics and Reliability Sciences.